Mon. Not. R. Astron. Soc. **000**, 000–000 (0000) Printed 20 May 2016 (MN LATEX style file v2.2)

Intermediate-mass black holes from Population III remnants in the first galactic nuclei

Taeho Ryu[1⋆], Takamitsu L. Tanaka[1], Rosalba Perna[1,2], Zoltán Haiman[3]
[1]*Department of Physics and Astronomy, Stony Brook University, Stony Brook, NY 11794-3800, USA*
[2]*Fellow Adjoint of JILA, 440 UCB, Boulder, CO 80309-0440, USA*
[3]*Department of Astronomy, Columbia University, 550 W. 120th Street, New York, NY 10027, USA*

arXiv:1603.08513v2 [astro-ph.GA] 19 May 2016

20 May 2016

ABSTRACT

We report the formation of intermediate-mass black holes (IMBHs) in suites of numerical N-body simulations of Population III remnant black holes (BHs) embedded in gas-rich protogalaxies at redshifts $z \gtrsim 10$. We model the effects of gas drag on the BHs' orbits, and allow BHs to grow via gas accretion, including a mode of hyper-Eddington accretion in which photon trapping and rapid gas inflow suppress any negative radiative feedback. Most initial BH configurations lead to the formation of one (but never more than one) IMBH in the center of the protogalaxy, reaching a mass of 10^{3-5} $M_\odot$ through hyper-Eddington growth. Our results suggest a viable pathway to forming the earliest massive BHs in the centers of early galaxies. We also find that the nuclear IMBH typically captures a stellar-mass BH companion, making these systems observable in gravitational waves as extreme mass-ratio inspirals (EMRIs) with *eLISA*.

Key words: black hole physics, cosmology: theory, quasars: supermassive black holes, gravitational waves

1 INTRODUCTION

Virtually every nearby massive galaxy harbors a supermassive black hole (SMBH) in its nucleus (Kormendy & Ho 2013; Magorrian et al. 1996). Tight correlations between SMBHs and the properties of their host galaxies, as well as the phenomenology of quasars and luminous active galactic nuclei, suggest that SMBHs play a role in shaping their environment both on local (Silk & Rees 1998; Fabian 2012) and cosmological (Madau et al. 2004; Ricotti & Ostriker 2004; Tanaka, O'Leary & Perna 2016) scales.

How SMBHs form is one of the most fundamental open problems in astrophysics. The observation of quasars powered by $\sim 10^9$ $M_\odot$ SMBHs at $z \approx 6-7$, less than a Gyr after the Big Bang (Fan et al. 2001; Willott, McLure & Jarvis 2003; Willott et al. 2010; Mortlock et al. 2011; Venemans et al. 2013), places strong constraints on theoretical models for their origin (see reviews by, e.g. Volonteri 2010; Haiman 2013). The two most often discussed hypotheses are that they grew from either (i) the stellar BH remnants of the first generation of ~ 100 $M_\odot$ stars (Population III, hereafter Pop III, stars; Haiman & Loeb 2001; Madau & Rees 2001; Yoo & Miralda-Escudé 2004; Volonteri & Rees 2006; Tanaka & Haiman 2009), or (ii) the remnants of the "direct collapse" of $> 10^5$ $M_\odot$ gas clouds that avoided fragmentation into Pop III stars (Oh & Haiman 2002; Bromm & Loeb 2003; Koushiappas, Bullock & Dekel 2004; Volonteri & Rees 2005; Shapiro 2005; Begelman, Volonteri & Rees 2006; Spaans & Silk 2006; Lodato & Natarajan 2006; Wise & Abel 2008; Regan & Haehnelt 2009a; Schleicher, Spaans & Glover 2010; Shang, Bryan & Haiman 2010; Latif et al. 2013; Tanaka & Li 2014). Both scenarios require that some of the first SMBHs grew at a (logarithmically averaged) rate $\dot{M} \sim 10 L_{\rm Edd}/c^2$ (e.g. Tanaka 2014), where $L_{\rm Edd} \propto M$ is the Eddington luminosity for a BH of mass M, and c is the speed of light. This value is comparable to the accretion rate producing the Eddington luminosity with the radiative efficiency $\eta \equiv L/(\dot{M}c^2) \sim 0.1$ expected in thin discs.[1]

In this paper, we examine the possibility that the first nuclear SMBHs originated from *hyper-Eddington* accretion onto Pop III remnants—i.e. from a growth mode where $\dot{M} \gg \dot{M}_{\rm Edd} \equiv L_{\rm Edd}/c^2$. This is motivated by theoretical models of optically thick accretion flows in which photons are trapped and advected inside the accretion flow. In such "radiatively inefficient" accretion modes the luminosity and

⋆ email: taeho.ryu@stonybrook.edu

[1] Radiatively efficient discs are theoretically expected to have $\eta \sim 0.1 - 0.4$ (e.g. Shapiro 2005), in agreement with the mean value $\sim 0.07 - 0.1$ inferred from the Sołtan-Paczynski argument, comparing the mass density of SMBHs with the quasar luminosity density (e.g. Merloni & Heinz 2008; Shankar et al. 2010, but see Shankar et al. 2016 for a recent argument for a higher value).

© 0000 RAS

radiation feedback of the flow are quenched, allowing accretion rates much higher than those corresponding to the Eddington limit for radiatively efficient discs (see Begelman 1979 for spherical flows and Abramowicz et al. 1988 for slim accretion discs). Several studies have investigated whether such an accretion mode contributed to the growth of the first SMBHs (Volonteri & Rees 2005; Begelman 2012; Madau, Haardt & Dotti 2014; Alexander & Natarajan 2014; Volonteri, Silk & Dubus 2015; Pacucci & Ferrara 2015; Pacucci, Volonteri & Ferrara 2015; Lupi et al. 2016; Pezzulli, Valiante & Schneider 2016).

We focus our attention on the recent work by Inayoshi, Haiman & Ostriker (2015, hereafter IHO16), who found hyper-Eddington accretion solutions in spherically symmetric radiation-hydrodynamics simulations of Bondi-like accretion. They found, in broad agreement with previous simulations (Milosavljević et al. 2009; Park & Ricotti 2012), that radiative feedback typically limits the accretion rate to values comparable or below $\dot{M}_{\rm Edd}$. This radiative feedback arises from photoionization and heating of the gas near the Bondi radius, and occurs even for flows that are highly optically thick to electron scattering, and for which trapping of the radiation limits the luminosity emerging from the photosphere below $L_{\rm Edd}$. However, IHO16 also found that for sufficiently large ambient gas densities, the combination of the large ram pressure of the inflowing gas and photon trapping inhibit radiative feedback. The accretion flow in this regime is steady and unimpeded from the Bondi rate; following IHO16 we refer to this as hyper-Eddington accretion.

We perform N-body simulations of Pop III remnant BHs in a model protogalactic distribution of gas and dark matter (DM) at $z \gtrsim 10$, subjecting the BHs to dynamical friction, and allowing them to accrete in the manner found by IHO16. The goal of our simulations is to follow the coupled growth and orbital evolution of a small cluster of stellar-remnant BHs, and to evaluate whether such BHs can reasonably be expected to reach the hyper-Eddington regime, and grow rapidly into more massive BHs.

In our models, we find that Pop III BHs indeed frequently grow into intermediate-mass black holes (IMBHs) with masses over 10^3 $\rm M_\odot$, and even into supermassive holes (SMBHs) with masses 10^5 $\rm M_\odot$. We further find that these I/SMBHs always form after a lower-mass BH has eroded its orbit, and settled near the center of the model protogalaxy. This suggests that hyper-Eddington accretion is a viable mechanism for forming nuclear SMBHs in early galaxies.

In addition, we report that our simulations always produce only a single I/SMBH. This is because once these massive BHs dominate the central potential, subsequent BHs dragged into the dense central regions reach high velocities that prohibit their growth. Instead, they are captured as stellar-mass BHs in a bound orbit. This suggests that I/SMBH formation is typically accompanied by so-called extreme-mass ratio inspirals (EMRIs), the merger of compact objects with mass ratios $\ll 1$ that are one of the main targets of the planned space-borne gravitational-wave detector *eLISA*.

The rest of this paper is organized as follows. In §2, we describe the setup of our simulations, including the properties of the Pop III remnant BHs and of their host galaxy, as well as the numerical schemes used to simulate their orbital evolution and growth. We present and discuss our main results in §3. Several implications and theoretical caveats are discussed further in §4. We summarize our conclusions in §5.

2 NUMERICAL MODEL

In this section, we provide an overview of our simulations. We first describe the properties of the parent galaxy, and the initial conditions for the small cluster of stellar-mass BHs. We then describe the equations of motion we solve to follow the growth of BHs and their interactions and dynamics, as well as the numerical scheme we use to solve these equations. A key feature of our model is a prescription that allows rapid growth by gas accretion, based on the recent numerical study of Bondi-like hyper-Eddington accretion with radiation by IHO16.

2.1 Protogalaxy + BH population model

2.1.1 Protogalactic gas cloud and DM halo

We consider a small cluster of Pop III-remnant BHs embedded in a protogalactic, so-called atomic-cooling DM halo, with a virial temperature of $T_{\rm vir} \geqslant 10^4$K and mass $\gtrsim 10^{7-8}$ $\rm M_\odot$ at $z \sim 15-20$. Such a system is a plausible outcome of lower-mass Pop III-forming haloes growing either via accretion and minor mergers, or via major mergers. Massive stars are expected to form earlier, in the lower-mass progenitor "minihaloes", and leave behind stellar-mass BH remnants. However, the UV radiation and/or supernova (SN) explosions of the progenitor star of such a BH can unbind the gas from the shallow potential well of its host minihalo. The remnant BHs are then expected to be starved (e.g. Alvarez, Wise & Abel 2009), and not surrounded again by dense gas and grow until they are incorporated into more massive atomic-cooling haloes.

The gas collapsing inside an atomic cooling halo is expected to cool and condense, and to develop a nearly isothermal density profile with $\mathrm{d}\ln\rho/\mathrm{d}\ln r \approx -2$ (Oh & Haiman 2002; Wise & Abel 2007; Regan & Haehnelt 2009b; Shang, Bryan & Haiman 2010; Latif, Schleicher & Schmidt 2014; Regan, Johansson & Haehnelt 2014). Under the assumption that the metallicity in this protogalaxy remains low, and H_2 cooling is disabled, the temperature will remain near the HI atomic cooling floor of 8000 K. This configuration is expected to be rare, as it requires a large UV (Lyman-Werner) flux from a bright neighbour, forming near-simultaneously (Dijkstra et al. 2008; Agarwal et al. 2012; Visbal, Haiman & Bryan 2014). In the presence of metal and/or H_2-cooling, the large-scale inflow rate is expected to be slower, as a result of the lower sound speed, reducing the normalization of the density profile (see, e.g. Shang, Bryan & Haiman 2010).

Our fiducial protogalaxy model is based on the metal- and H_2–free atomic cooling halo, and consists of a DM component with a Navarro, Frenk & White (1997) (NFW) density profile, and an isothermal gas profile that behaves as $\propto r^{-2}$ at large radii. In order to avoid a mathematical singularity at the origin, we introduce a core region of size $r_{\rm c}$ inside which the density is nearly constant.

The matter distribution in our model protogalaxy can

Redshift	$z \approx 15 - 20$
Sound speed	$c_{\rm s} \approx 10$ km s^{-1}
Halo mass	$M_{\rm vir,halo} \approx 5 \times 10^7 - 10^8$ M$_\odot$
Halo virial temperature	$T_{\rm vir} \gtrsim 10000$ K
Initial radial distance of BHs	$r_i(t=0) \leqslant 100$ pc
Initial separations between BHs	$r_{ij}(t=0) \geqslant 10$ pc
Initial speed of BHs	$v_i(t=0) \leqslant c_{\rm s}$
Mean molecular weight	$\mu_{\rm m} = 1$
Gas density profile	$\rho_{\rm gas} \propto r^{-2}$ (isothermal sphere)
Dark matter density profile	$\rho_{\rm DM}$=NFW
Concentration parameter	C=9
Virial radius	$r_{\rm vir} \simeq 1$ kpc
Core gas density	$n_{\rm c} = 2.5 \times 10^{10}$ cm^{-3}
Core radius for gas	$r_{\rm c} = 3 \times 10^{-3}$ pc
Core radius for DM	$r_{\rm NFW,c} \approx 10^{-6}$ pc
Initial stellar mass function range	25 M$_\odot$ $\leqslant M_\star \leqslant$ 140 M$_\odot$
Initial stellar mass function slope	$\alpha = 0.17$
Total run time	$t_{\rm run} = 500$ Myrs

Table 1. Choices of the values of different physical parameters defining our protogalaxy + BH cluster model. See text for details. Note that the italic subscripts i and j are indices representing the BHs.

be summarized as follows:

$$\rho_{\rm bg}(r) = \rho_{\rm gas}(r) + \rho_{\rm NFW}(r) \quad (1)$$

$$\rho_{\rm gas}(r) = \frac{\rho_{\rm c}}{1 + (\frac{r}{r_{\rm c}})^2}, \quad (2)$$

where $\rho_{\rm NFW}(r)$ is the NFW profile with concentration parameter $C = 9$ and the virial radius is $r_{\rm vir} \simeq 1$ kpc. The virial radius is defined as the radius within which the average matter density is 180 times the cosmological critical density. The values of $r_{\rm c}$ and $n_{\rm c}$ are determined by normalizing the gas profile to satisfy the cosmological ratio of baryon to DM mass inside $r_{\rm vir}$. We take $r_{\rm c} = 0.003$ pc and $n_{\rm c} = 2.5 \times 10^{10}$cm^{-3}. These values are consistent with those found in the highest-resolution adaptive mesh refinement simulations to date (Regan, Johansson & Haehnelt 2014). For numerical convenience, we slightly modify the NFW profile (which scales as r^{-1} at small radii) by requiring that the DM density does not exceed the gas density for $r \leqslant r_{\rm NFW,c}$, a radius at which $\rho_{\rm gas} = \rho_{\rm NFW}$. This modification only affects the region inside $\sim 10^{-3} r_{\rm c}$, and does not appreciably affect our results. The density profile of DM and gas remains fixed and unchanging throughout our simulations; the possible impact of this large simplification is addressed below.

2.1.2 Pop III-remnant BHs

Within our spherically symmetric halo, we place a small cluster of ten BHs inside a radius of 100 pc. This represents $\approx 10\%$ of the virial radius of a halo just above the atomic cooling threshold, and is intended to correspond to the spatial extent of a star-forming region, or the region over which the BHs are initially spread after merging events. Each hemisphere is divided by the polar angle into five compartments of equal shape and size, and a single BH is placed at a randomly chosen radius and angular position inside each compartment (i.e., ten compartments, and one BH per compartment).

We also require that the initial distance between each pair of BHs is larger than 10 pc. Each BH is given a random initial velocity, so that its speed is no larger than the gas sound speed $c_{\rm s} \approx 10\,{\rm km\,s^{-1}}$ and the radial component of its velocity is nonpositive (i.e. it is not flying away from the origin; this is intended to mimic the outcome of recent mergers).

The masses of the Pop III stars as the BH progenitors are assigned randomly from an initial mass function (IMF) $\frac{dN}{dM_\star} = M_\star^{-\alpha}$ with $\alpha = 0.17$ (Stacy & Bromm 2013). We adopt a minimum mass of $M_{\rm min,\star} = 25$ M$_\odot$, and a maximum mass of $M_{\rm max,\star} = 140$ M$_\odot$. The latter value is motivated by the fact that more massive stars are expected to result in pair-instability supernovae and leave no BH remnant (Heger et al. 2003). While stars more massive than ≈ 260 M$_\odot$ may form BHs, such large masses may be precluded by UV feedback in the protostellar stages (e.g. Hosokawa et al. 2011).

After the stellar masses are drawn, they are converted to BH masses M using the following fitting formulae provided by Tanaka, Perna & Haiman (2012), which are based on simulations by Zhang, Woosley & Heger (2008):

$$M = \begin{cases} \frac{3}{4}(M_\star - 20\ {\rm M}_\odot) + 2\ {\rm M}_\odot & \text{if } M_\star \leqslant 45\ {\rm M}_\odot \\ \frac{5}{12}(M_\star - 20\ {\rm M}_\odot) & \text{if } M_\star > 45\ {\rm M}_\odot\,. \end{cases} \quad (3)$$

The average mass of a Pop III star is $\langle M_\star \rangle \approx 80$ M$_\odot$, and that of a remnant BH is $\langle M \rangle \approx 25$ M$_\odot$. All simulations are run until either a tightly bound BH pair with a semimajor axis $a \leqslant 1$ pc forms, or until a physical time of $t_{\rm run} = 500$ Myr has elapsed—whichever occurs first.

The properties of the host halo and the BHs adopted in our simulations are summarized in Table 1, and a schematic diagram of the halo + BH system is illustrated in Figure 1. The radial coordinate of the BH is denoted by r. The gas density profile is spherically symmetric, and has a flat central core of size $r_{\rm c}$. The sum of the gas and DM densities define the total background matter density $\rho_{\rm bg}$. We denote the mass enclosed inside the instantaneous radial coordinate of the BH by $M_{\rm bg}(< r)$. The Bondi radius $r_{\rm B}$ (defined in §2.3 below) defines a spherical region around each BH that we call the "Bondi sphere." We will make use of the average density around the surface of this sphere, $\langle \rho \rangle_{\rm B}$, and the total mass enclosed inside the Bondi sphere, $M_{\rm B}$.

2.2 The equations of motion

We use an N-body code to integrate the equations of motion and mass growth for each BH embedded in the model protogalaxy. The motion of the BHs is determined by the following forces: (i) their mutual gravitational attraction (including post-Newtonian terms up to 2.5th order), (ii) dynamical friction/drag from the surrounding medium, and (iii) the gravitational potential of the background matter. We also account for (iv) the deceleration due to mass growth via accretion. The resulting equation of motion for the $i^{\rm th}$ BH

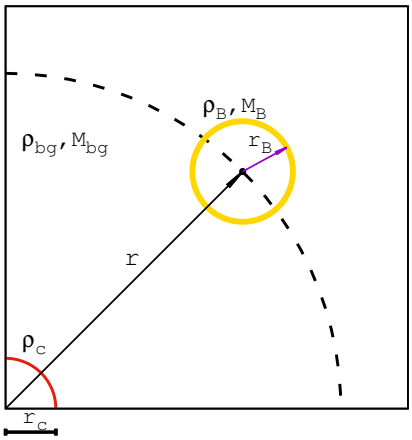

Figure 1. Schematic representation of one of the BHs in the halo, defining our notation. $M_{\rm bg}(< r)$ denotes the mass of the background material (gas + DM) enclosed within the radial position r of the BH, while $M_{\rm B}$ represents the mass of gas enclosed within the Bondi radius of the BH.

includes the sum of the five forces:

$$\mathbf{a}_i = \mathbf{a}_{{\rm N},i} + \mathbf{a}_{{\rm PN},i} + \mathbf{a}_{{\rm df},i} + \mathbf{a}_{{\rm bg},i} + \mathbf{a}_{{\rm acc},i} \qquad (4)$$

This equation is iteratively integrated at every time step, and used to update the positions and velocities with the N-body algorithm described in § 2.4 below. We next describe each contribution in detail.

(i) *Gravitational attraction between BHs*
This contribution is dominated by the standard Newtonian expression,

$$\mathbf{a}_{{\rm N},i} = -\sum_{j\neq i} G\ M_{{\rm BH},j}\ \frac{\partial\ \Phi(r_{ij})}{\partial\ r_{ij}}\ \frac{\mathbf{r}_i - \mathbf{r}_j}{r_{ij}}, \qquad (5)$$

where G is the gravitational constant, Φ is the pairwise gravitational potential, $\mathbf{r}_i$ is the displacement of the $i^{\rm th}$ BH from the center of the host DM halo, and $r_{ij} \equiv |\mathbf{r}_i - \mathbf{r}_j|$. In our numerical implementation, we adopt the Plummer softening kernel (e.g. Binney & Tremaine 1987) with softening length 1.7×10^6 cm, which is equivalent to the Schwarzschild radius for a 5.75 $\rm M_\odot$ BH.

We add post-Newtonian terms $\mathbf{a}_{\rm PN}$ to Eq. (5) up to order 2.5, which includes the loss of orbital energy and angular momentum via gravitational waves (GWs). The full expressions for these terms can be found in, e.g., Kupi, Amaro-Seoane & Spurzem (2006, see also Damour & Deruelle 1981). At sufficiently small pair separations, the orbital decay due to GW emission leads to merger on a timescale $\propto a^4$ where a is the semimajor axis (Peters & Mathews 1963; Peters 1964). It turns out that no BHs in our simulations reach separations where GW emission is relevant for their orbital evolution[2] Notice that This finding is different from the similar, earlier studies by Tagawa et al. (2015); Tagawa, Umemura & Gouda (2016), who considered a cluster of BHs with a smaller initial separation, and found that the post-Newtonian terms can sometimes be important and lead to BH-BH mergers. We defer the discussion of this point to § 4 below.

[2] For reference, GW emission becomes the dominant orbital evolution mechanism at an orbital distance $a < 10^{-5}$ pc for a circular binary consisting of two BHs with masses 10^5 $\rm M_\odot$ and 100 $\rm M_\odot$. We find that the central pair is rarely disrupted once they reach a separation ~ 1 pc, as described later in the text (§3.3).

(ii) *Dynamical friction and gas drag*
An object in motion through a medium creates an overdensity, or wake, behind it, whose gravitational pull acts as a dissipative drag on the object's motion. In this study, we consider dynamical friction due to both DM and gas.

For the DM contribution, we adopt the standard Chandrasekhar formula(Binney & Tremaine 1987),

$$\mathbf{a}^{\rm (DM)}_{{\rm df},i} = -4\pi\ \ln\Lambda\ f(X_i)\ \frac{G^2 M_i}{v_i^3}\ \rho_{\rm DM}(r_i)\ \mathbf{v}_i, \qquad (6)$$

with

$$f(X_i) \equiv {\rm erf}(X_i) - \frac{2}{\sqrt{\pi}}\ X_i\ \exp\left(-X_i^2\right), \qquad (7)$$

where $X_i \equiv v_i/(\sqrt{2}\sigma_v)$ and σ is the velocity dispersion, $\simeq c_{\rm s}$. We use $\ln\Lambda = 3.1$ and indicate with $\rho_{\rm DM}(r_i)$ the DM density at the location of the i-th BH.

For the gas, we adopt the following formula from Tanaka & Haiman (2009), which incorporates behaviours found in numerical simulations for subsonic and supersonic regimes (Ostriker 1999; Escala et al. 2004; Chapon, Mayer & Teyssier 2013). In our implementation, the specific drag force vector always points opposite to the direction of BH motion, and is given by:

$$\mathbf{a}^{\rm (gas)}_{{\rm df},i} = -4\pi\ G^2\ M_i\ \rho_{\rm gas}(r_i)\ \frac{1}{v_i^3} \times f^{\rm (gas)}(\mathcal{M}_i)\mathbf{v}_i, \qquad (8)$$

with

$$f^{\rm (gas)}(\mathcal{M}_i) = \begin{cases} 0.5\ \ln\Lambda\left[{\rm erf}\left(\frac{\mathcal{M}_i}{\sqrt{2}}\right) - \sqrt{\frac{2}{\pi}}\mathcal{M}_i\ \exp\left(-\frac{\mathcal{M}_i^2}{2}\right)\right] \\ \qquad\qquad 0 \leqslant \mathcal{M}_i \leqslant 0.8; \\ 1.5\ \ln\Lambda\left[{\rm erf}\left(\frac{\mathcal{M}_i}{\sqrt{2}}\right) - \sqrt{\frac{2}{\pi}}\mathcal{M}_i\ \exp\left(-\frac{\mathcal{M}_i^2}{2}\right)\right] \\ \qquad\qquad 0.8 \leqslant \mathcal{M} \leqslant \mathcal{M}_{\rm eq}; \\ \frac{1}{2}\ln\left(1-\frac{1}{\mathcal{M}_i^2}\right) + \ln\Lambda \\ \qquad\qquad \mathcal{M}_i > \mathcal{M}_{\rm eq}. \end{cases} \qquad (9)$$

Above, $\mathcal{M}_i \equiv v_i/c_{\rm s}$ is the Mach number of the ith BH, and $c_{\rm s}$ is the isothermal sound speed of the gas. We use $\ln\Lambda = 3.1$, the same as for the DM. The corresponding value of $\mathcal{M}_{\rm eq}$ that makes the above function continuous with respect to $\mathcal{M}$ is approximately 1.8.

With the density distributions we use in our model (see § 2.1 above), and in particular near the center of the model protogalaxy, the effects of gas dominate over that of DM—both in dynamical friction and background gravitational force. Although we include the DM-related force calculations for completeness, they do not play a major dynamical role.

The expressions for dynamical friction given above were derived under the assumption of non-accelerated motion in a uniform density distribution. Capturing the effects of nonlinear dynamical friction along an accelerated trajectory, in a non-uniform background medium, would require hydrodynamical simulations, including the self-gravity of the surrounding medium. This is outside the scope of this

paper, but we note that existing studies of dynamical friction in a nonuniform medium or for perturbers on nonlinear trajectories (e.g Sánchez-Salcedo & Brandenburg 2001; Just & Peñarrubia 2005; Kim & Kim 2007; Kim 2010), do not report major differences from the Chandrasekhar formula. We therefore simply evaluate the formulae given above, by using the value of the density at the coordinates of each BH; this is the typical approach taken in similar numerical studies (e.g. Blecha et al. 2011; Guedes et al. 2011). For comparison, we have run a second set of simulations in which the dynamical friction forces were computed by averaging the density values at a distance around each BH; we defer discussing the details of this comparison until §2.5 below.

(iii) *Gravity of the background matter*
The background gas and DM exert a gravitational pull on the BHs. Because we assume a spherically symmetric density profile, this force points toward the center of the potential. It can be expressed as

$$\mathbf{a}_{\rm bg,}{}_i = -\frac{G\ M_{{\rm bg},i}}{r_i^3}\mathbf{r}_i, \tag{10}$$

where $\mathbf{r}_i$ is vector pointing from the center of the halo to the i-th BH and $M_{{\rm bg},i}$ is the mass of ambient gas and DM contained inside $r < r_i$.

Our assumption that the background matter distribution remains static will fail when $M \gtrsim M_{\rm bg}$, i.e. when the BH mass exceeds that of the matter inside its orbit. In this case, the matter at the center will be strongly perturbed by the BH, and our prescription of a static background is invalidated. Treating the dynamical reaction of the gas and DM distribution to a massive BH is beyond the scope of our computational methods. However, in order to assess the possible impact of this assumption on our results, we have run two sets of simulations with different treatments of the background force. In the first set, we treat this force simply as given by equation 10. In the second, we set it to zero if $M > M_{\rm bg}$. The full set of our simulations is described in §2.5.

(iv) *Accretion-induced deceleration*
The BH decelerates through conservation of linear momentum,

$$\mathbf{a}_{{\rm acc},i} = -\frac{\dot{M}_i}{M_i}\mathbf{v}_i. \tag{11}$$

2.3 Accretion rate

We next detail our prescription for the mass growth of each BH due to gas accretion. We base our model on the recent numerical study by IHO16, whose key finding is that the accretion rate can significantly exceed the Eddington rate (see also the other references mentioned in the Introduction). IHO16 found that spherically symmetric BH accretion solutions with radiative feedback were divided into several qualitatively distinct regimes, depending on the ratio of the Bondi accretion rate of ambient gas (ρ_∞),

$$\dot{M}_{\rm B} = \frac{4\pi G^2 M^2\ \rho_\infty}{c_{{\rm s},\infty}^3}, \tag{12}$$

($c_{{\rm s},\infty}$ being the sound of speed of the ambient gas), to the Eddington rate[3]

$$\dot{M}_{\rm Edd} \equiv \frac{L_{\rm Edd}}{c^2} = \frac{4\pi G M}{\kappa_{\rm es}\ c} = 2.2\times10^{-9}\,\frac{M}{{\rm M}_\odot}\ {\rm M}_\odot\ {\rm yr}^{-1}, \tag{13}$$

where $L_{\rm Edd}$ is the Eddington luminosity and $\kappa_{\rm es}$ is the Thomson scattering opacity.

IHO16 concluded that:
(i) Under conditions where the ratio of the canonical Bondi rate to the Eddington rate $\dot{M}_{\rm B}/\dot{M}_{\rm Edd} \lesssim 0.1-1$, the BH accretion rate is $\dot{M} \sim \dot{M}_{\rm B}$;
(ii) If $1 \lesssim \dot{M}_{\rm B}/\dot{M}_{\rm Edd} \lesssim 100$, photoionization by the light produced by the accretion flow causes the accretion onto the BH to be intermittent, with a time-averaged rate $\dot{M} \lesssim \dot{M}_{\rm Edd}$;
(iii) If $\dot{M}_{\rm B}/\dot{M}_{\rm Edd} \gtrsim 3000$, the large ram pressure of the inflowing gas, combined with photon trapping below the photosphere, renders radiative feedback ineffective, and accretion proceeds unimpeded at $\dot{M} \sim \dot{M}_{\rm B}$ (cf. Begelman 2012).
In the intermediate regime between cases (ii) and (iii) above, i.e. if $100 \lesssim \dot{M}_{\rm B}/\dot{M}_{\rm Edd} \lesssim 3000$, the accretion rate remains uncertain, because of the unresolved role of hydrodynamical instabilities.

Our accretion prescription closely follows the behaviour outlined above, with a few modifications. First, we replace the Bondi rate for a stationary mass with the Bondi-Hoyle-Lyttleton (BHL) rate, to account for the fact that the BHs in our simulation are in motion with respect to the surrounding gas. Second, whereas the canonical expression for the Bondi accretion rate (eq. 12) uses the ambient density "at infinity" ρ_∞, we instead use the value of the density averaged over the spherical region around the BH defined by the Bondi radius

$$r_{{\rm B},i} = \frac{2GM_i}{c_{\rm s}^2 + v_i^2}. \tag{14}$$

The resulting expression for our modified Bondi rate is

$$\dot{M}_{{\rm B},i} = \frac{4\pi G^2 M_i^2\ \langle\rho_{\rm B}(r_i)\rangle}{c_{\rm s}^3(1+\mathcal{M}_i^2)^{3/2}}, \tag{15}$$

where $\langle\rho_{\rm B}(r_i)\rangle$ denotes the aforementioned average density of gas at the surface of the "Bondi sphere" around the BH.

Third, we conservatively assume that the BH accretion rate should not be higher than the mass inflow rate into the center of the halo from larger scales, as this would deplete the central gas density, without the possibility of a steady replenishment from larger radii. In pristine atomic–cooling haloes, the hydrodynamical simulations mentioned above typically find this inflow rate to be

$$\dot{M}_{\rm in} = \frac{c_{\rm s}^3}{G} \approx 0.5\ {\rm M}_\odot\ {\rm yr}^{-1}. \tag{16}$$

A possible caveat here is that the inflow rate in the presence of metal and/or H_2 cooling may be ≈ two orders of magnitude lower. On the other hand, the rate increases steadily as the halo grows in mass, and recent simulations have found that pressure and gravitational torques can maintain $\sim$ ${\rm M}_\odot$ yr^{-1} inflow rates down to ∼pc scales, even in the

[3] Our notation was chosen to match that of IHO16. Many other works define $\dot{M}_{\rm Edd}$ to correspond to the Eddington luminosity with a radiative efficiency of η, which would be $\dot{M}_{\rm Edd}/\eta$, i.e. a factor of 10 higher than eq. (13) for $\eta = 0.1$.

face of radiative cooling and SN feedback (Prieto & Escala 2015).

Our implementation of the IHO16 accretion regimes can therefore be summarized as:

$$\dot{M} = \begin{cases} \min[\dot{M}_{\rm B}, \frac{1}{\eta}\dot{M}_{\rm Edd}, \dot{M}_{\rm in}] \\ \qquad (\text{if } \min[\dot{M}_{\rm B}, \dot{M}_{\rm in}] < 3000\dot{M}_{\rm Edd}) \\ \\ \min[\dot{M}_{\rm B}, \dot{M}_{\rm in}] \\ \qquad (\text{if } \min[\dot{M}_{\rm B}, \dot{M}_{\rm in}] \geqslant 3000\dot{M}_{\rm Edd}) \end{cases} . \quad (17)$$

In this study, we take $\eta = 0.1$. We note that this may somewhat overestimate the accretion rate in the Eddington-limited regime, as both Park & Ricotti (2012) and IHO16 found that the time-averaged rate is limited to $\sim 0.5\dot{M}_{\rm Edd}$. We implement Equation (17) as long as the BH dominates the gravitational potential inside its Bondi sphere, i.e. $M > M_{\rm B}$. On the other hand, if $M < M_{\rm B}$, the Bondi formalism breaks down. The latter condition roughly coincides with the gas inside the Bondi sphere becoming self-gravitating and Jeans-unstable. In this regime, the accretion rate is plausibly of order $\dot{M}_{\rm in} \approx c_{\rm s}^3/G$. However, how much of this canonical inflow rate ends up accreting onto the BH remains uncertain, and will depend on factors such as gas cooling, turbulence and angular momentum transport, and the BH's specific accelerated trajectory. We here parameterize the accretion rate in this self-gravitating gas regime as $\dot{M} = f_{\rm in}\dot{M}_{\rm in}$, and consider the two extreme values of $f_{\rm in} = 0$ and 1, as well as an intermediate value of $f_{\rm in} = 10^{-3}$.

To further explore the dependence of our results on this accretion prescription, we have also run a set of simulations where $\dot{M}$ continues to be given by the Bondi rate even when $M_{\rm B} > M$, and another set where $\dot{M}$ continues to follow the IHO16 prescription described above, regardless of whether $M_{\rm B}$ is larger or smaller than M.

2.4 Code Description

We perform 3-dimensional N-body simulations with a 4th-order, 5-stage Runge-Kutta-Fehlberg method (RKF45 method, Erwin 1969), using adaptive time steps. RKF45 is a highly accurate and stable integration method among the large class of Runge-Kutta schemes, particularly by adapting the Butcher tableau for Fehlberg's 4(5) method.

We solve equation (4) as described in the preceding text, and at each time step we update the components of the position, velocity and acceleration, as well as the masses of the BHs, according to prescribed forces and accretion rates. To ensure numerical precision, our computational scheme varies the value of each subsequent time step analytically, so that numerical errors for each variable in the simulation do not exceed 10^{-13} times the size of the variable. In some cases, however, this algorithm can spend an excessive amount of time calculating trivial interactions. In order to avoid such situations and to achieve acceptable code speeds, we implement a shortcut in the form of a minimum time step,

$$\Delta t_{\rm short} = 10^{-6} \times \min\{\tau_{{\rm dyn},ij}, \tau_{{\rm df},i}, M_i/\dot{M}_i, v_i/a_i\}, \quad (18)$$

where $\{\tau_{{\rm dyn},ij}\}$ is the set of dynamical times evaluated for each BH pair, as well as for each BH and the background potential; $\tau_{{\rm df},ij}$ is the timescale for orbital energy dissipation by dynamical friction and gas drag for each BH pair; $M_i/\dot{M}_i$ is the accretion timescale, and v_i/a_i is the ratio of the speed to the net acceleration for each BH.

The main body of the code is the same as the one that was used in Ryu, Tanaka & Perna (2016). We refer the reader to that paper for further details.

2.5 Summary of simulation sets

Our fiducial set of models implement the prescriptions described above. The accretion rate onto the BH is determined by the IHO16 accretion rates (eq. 17) if $M > M_{\rm B}$, and $\dot{M} = f_{\rm in}M_{\rm in}$ in the self-gravitating regime, once $M \leqslant M_{\rm B}$. As noted above, we have run two additional sets of simulations, in which $\dot{M}$ is either given by Eq. (17) regardless of how M compares to $M_{\rm B}$ (which we will refer to as (Prescription "I"; for Inayoshi et al.) and another in which BH accretion tracks the Bondi rate, but is always Eddington-limited, i.e. $\dot{M} = \min[\dot{M}_{\rm B}, \frac{1}{\eta}\dot{M}_{\rm Edd}, \dot{M}_{\rm in}]$ (Prescription "E", for Eddington). Note that the latter is a prescription commonly adopted in numerical and semi-analytic studies of BH growth in the early Universe (see reviews by, e.g. Volonteri 2010; Haiman 2013 and references therein) As a simple control, we have also run simulations with no accretion.

For each of the six accretion prescriptions listed above, we consider a case where the background gravitational force $a_{{\rm bg},i}$ is always present and points inward. We then consider a second case, motivated in the previous subsection, where $a_{{\rm bg},i}$ is set to zero whenever the BH is more massive than the mass enclosed inside its present position [i.e. if $M_i > M_{\rm bg}(r_i)$].

Our full suite of simulations is summarized in Table 2. Each of the twelve models we have described above (six different accretion prescriptions, and two different treatments of the background gravitational force at small radii) were simulated multiple times using different initial values for BH masses, positions, and velocities (the criteria for our initial conditions are described in §2.1.2 and 1). We simulated each model using 43 distinct sets of initial conditions; each set of initial conditions was recycled 12 times, using the different prescriptions in the 12 different models.

3 RESULTS

We now turn to the results of our N-body simulations. We briefly summarize our major findings below, and follow these with detailed explanations and analyses.

(i) We found that in a majority (24 out of 43) of initial condition sets, an IMBH of mass $\sim 10^3$ to $\sim 10^5$ $M_\odot$ formed as a result of hyper-Eddington accretion, in all the models that allowed for this accretion mode (i.e. in models "$f_{\rm in} = 1$","$f_{\rm in} = 10^{-3}$","$f_{\rm in} = 0$" and "I" listed in Table 2).

(ii) If one set of initial conditions results in IMBH formation in one hyper-Eddington model, then it does so in all the others. The determining factor is whether the BH passes through a dense, gas-rich region (as a result of small semi-major axis, small pericenter, or both) where dissipation of orbital energy via gas drag is efficient.

(iii) All of the IMBHs end up within the central $\lesssim 0.01$ pc of the protogalactic halo, strongly suggesting that they are viable precursors of nuclear SMBHs observed as quasars at $z > 6$.

Table 2. Summary of our 6 prescriptions for BH accretion and 2 different treatments of the central background potential adopted in our simulations. These constitute a set of 12 models. Note that the accretion prescription in Eq. 17 follows IHO16. In model "I" this prescription is adopted independently of whether the BH mass exceeds or not the mass contained within its Bondi radius, $M_{\rm B}$, whereas in the "$f_{\rm in}$" models the accretion rate is capped to a fraction $f_{\rm in}$ of the inflow rate in the self-gravitating regime, when $M_{\rm B} \geqslant M$. Model "E" denotes a commonly adopted Eddington-limited accretion prescription, and in the $\dot{M} = 0$ reference case we do not allow any accretion.

Model		$\dot{M}$ when $M_{\rm B} < M$	$\dot{M}$ when $M_{\rm B} \geqslant M$
Accretion Prescription	$f_{\rm in} = 1$	eq.17	$\dot{M} = f_{\rm in}\dot{M}_{\rm in} = \dot{M}_{\rm in}$
	$f_{\rm in} = 10^{-3}$	eq.17	$\dot{M} = 10^{-3} \times \dot{M}_{\rm in}$
	$f_{\rm in} = 0$	eq.17	$\dot{M} = 0$
	I	eq.17	eq.17
	E	$\min[\dot{M}_{\rm B}, \frac{1}{\eta}\dot{M}_{\rm Edd}, \dot{M}_{\rm in}]$	$\min[\dot{M}_{\rm B}, \frac{1}{\eta}\dot{M}_{\rm Edd}, \dot{M}_{\rm in}]$
	$\dot{M} = 0$	$\dot{M} = 0$	$\dot{M} = 0$
Background Potential	On	$a_{{\rm bg},i}$ always on	
	Off	$a_{{\rm bg},i} = 0$ if $M_i > M_{\rm bg}(< r_i)$	

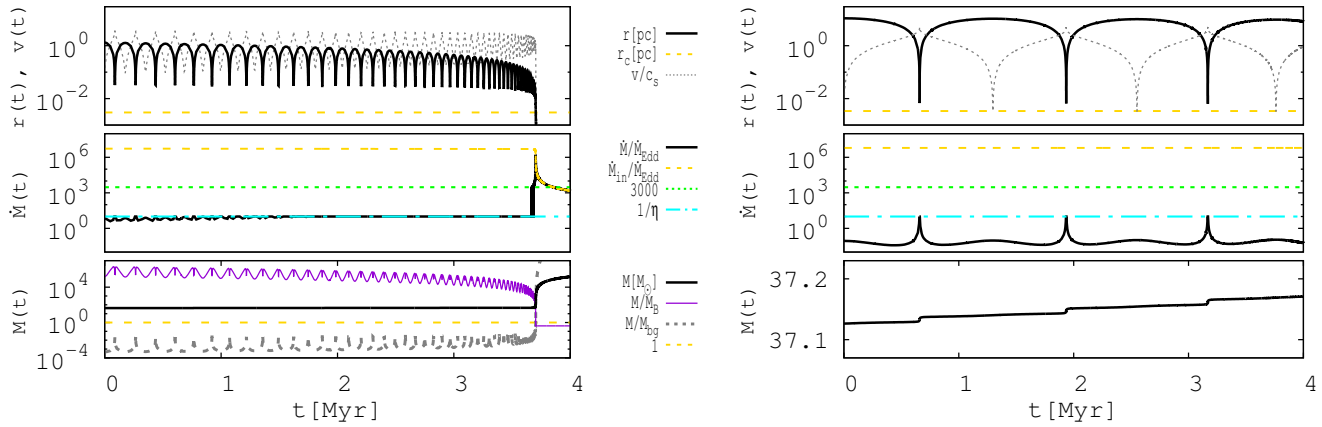

Figure 2. *Top left panel:* The radial distance r (black solid line), and Mach number (gray dotted line) of a BH which experiences the hyper-Eddington accretion as it sinks to the halo core, whose size $r_{\rm c}$ is also displayed for reference (yellow dashed line) in Model "$f_{\rm in} = 1$" with $a_{\rm bg}$ 'On' (see Table 2). *Middle left panel:* The corresponding accretion rate $\dot{M}$ of the BH in Eddington units (solid black line). For reference, the panel also shows the the self-gravitating inflow rate $\dot{M}_{\rm in}$ (yellow dashed) also in Eddington units, as well as the critical values at which the accretion switches modes [i.e. to Eddington (blue dot-dashed) or hyper-Eddington (green dotted)]. *Bottom left panel:* The corresponding mass of the BH is shown (solid black line), together with the mass $M_{\rm B}$ enclosed within its Bondi radius (solid magenta) and the gas mass $M_{\rm bg}$ contained inside its orbit (dashed gray). The accretion rate and the BH mass both grow rapidly once the BH sinks the core. At the same time, the BH begins to dominate the central potential, but not the mass inside its Bondi sphere. *Right panels:* The above behaviour is contrasted with a BH on a highly elliptical orbit but with a larger semimajor axis, which never makes it inside the core. This BH never experiences (hyper-)Eddington accretion, and its mass remains near its initial value.

(iv) There is at most one IMBH in each simulation; we do not find a single instance of multiple IMBHs forming.

(v) Many of the IMBHs capture a lighter BH into a close, sub-parsec orbit, and we argue that such systems could lead to EMRI events detectable by planned gravitational-wave observatories, such as *eLISA*.

(vi) We do not find mergers between stellar-mass BHs, in contrast to similar studies by Tagawa et al. (2015); Tagawa, Umemura & Gouda (2016). The main reason for this appears to be simply the larger radii at which we initially place the BHs.

(vii) The above findings appear to be robust with respect to our treatment of both dynamical friction and the gravitational force due to the background matter distribution.

3.1 The onset of hyper-Eddington accretion

The first significant event in our simulations is the descent of the innermost BH to the dense gaseous core, which is driven by the decay of its orbit due to dynamical friction. Because the BHs are relatively widely separated in our initial conditions (the initial mean separations are $\simeq 75$ pc), three-body interactions at this stage are rare. As the innermost BH sinks even closer to the center, its ambient density increases and its Bondi accretion rate increases. The accretion rate even-

tually transitions from $\dot{M} = \dot{M}_{\rm B} < \dot{M}_{\rm Edd}/\eta$ (sub-Eddington Bondi), to $\dot{M} = \dot{M}_{\rm Edd}/\eta < \dot{M}_{\rm B}$ (Eddington-limited), and finally (in 25 out of 43 cases) to $\dot{M} = \dot{M}_{\rm B} > 3000\ \dot{M}_{\rm Edd}$ (hyper-Eddington; accretion unimpeded by radiation feedback), as dictated by Eq. (17). This qualitative picture is shared by all of our simulations in which hyper-Eddington accretion occurs.

This progression is illustrated in the left panel of Figure 2, which shows the journey in position and mass for a BH that undergoes hyper-Eddington accretion. The data is taken from a simulation run using the $f_{\rm in} = 1$ accretion scenario and with the background gravitational force always present—however, we reiterate that the behaviour shown here is shared by all examples of hyper-Eddington accretion in our simulations.

The top left panel of this figure shows the position of the innermost BH with the core radius $r_{\rm c}$ shown for reference. In the middle panel, we show the BH accretion rate in units of $\dot{M}_{\rm Edd}$, alongside the two critical values that determine the accretion regime according to Eq. (17): 3000 $\dot{M}_{\rm Edd}$, and $\dot{M}_{\rm in}$. Finally, in the bottom panel, we show the mass M of the BH (in $\rm M_\odot$). We also plot $M/M_{\rm B}$, the ratio of the BH mass to the gas mass inside its Bondi sphere. Recall that when this ratio is greater than unity, we study evolution under different accretion prescriptions (the difference between our $f_{\rm in} = 1$, $f_{\rm in} = 10^{-3}$, $f_{\rm in} = 0$, and "I" models; see Table 3). Further, we show $M/M_{\rm bg}$, the ratio of the BH mass to the mass contained in the halo inward of the BH's radial position. If this ratio is greater than unity, we also study BH evolution without the background gravitational in the "Background Potential Off" simulations (see Table 3).

For comparison, on the right side of the figure, we have plotted the same information for another BH in the same simulation that does *not* undergo hyper-Eddington accretion. This BH is on a highly elliptical orbit around the center of the halo, but its Bondi accretion value never exceeds the $\dot{M}_{\rm B} = 3000\ \dot{M}_{\rm Edd}$ threshold to overcome radiative feedback.

In the left side of this figure, we see that it takes the accreting BH only a few Myr to sink to the center where it begins to undergo hyper-Eddington accretion. For BHs that undergo hyper-Eddington accretion in our simulations that allows this (models $f_{\rm in} = 1$, $f_{\rm in} = 10^{-3}$, $f_{\rm in} = 0$, and "I"), an average of 5.6 Myr elapses between when the Bondi accretion rate first reaches the Eddington limit and when it reaches $3000\dot{M}_{\rm Edd}$. This is much shorter than the Salpeter time (~ 45 Myr for the adopted radiative efficiency $\eta = 0.1$), indicating that the increase in the Bondi accretion rate is caused by the increase in ambient density ($\dot{M}_{\rm B} \propto \rho_{\rm gas} \propto r^{-2}$ for $r \gtrsim r_{\rm c}$), as opposed to mass growth ($\dot{M}_{\rm B} \propto M^2$).

In Figure 3, we show the semimajor axis (vertical axis) and eccentricity (plotted as $1-e$, horizontal axis) of each of our BHs in the "$f_{\rm in} = 1$, $a_{\rm bg}$ on" simulation set (a total of 43 runs and 430 BHs, 24 of which grow to become IMBHs). Because the BH orbits are not Keplerian (and therefore not elliptical), the concept of eccentricity is not rigorously defined. We evaluate the instantaneous eccentricity using the standard formula for Keplerian orbits

$$e = \sqrt{1 + \frac{2\epsilon\ell^2}{\{G[M + M_{\rm bg}(r)]\}^2}}, \qquad (19)$$

where ϵ is the specific energy of the orbit (orbital energy divided by the "instantaneous reduced mass" $M\ M_{\rm bg}(r)/[M + M_{\rm bg}(r)]$), and ℓ is the specific angular momentum (orbital angular momentum divided by the instantaneous reduced mass). Note that the gravitational potential used in calculating ϵ is logarithmic, and the enclosed central mass $M_{\rm bg}(r)$ varies with the orbital radius.

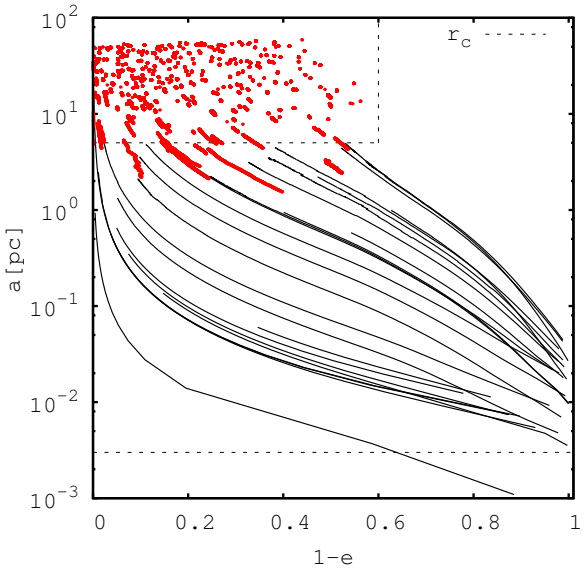

Figure 3. The evolution of the semimajor axis and eccentricity for 430 BHs in 43 simulations with the prescription "$f_{\rm in} = 1$, $a_{\rm bg}$ on." The BHs begin with large semimajor axes and high-eccentricity orbits (upper left of the panel). The red dots represent the orbits of 406 BHs that do not sink to the center within the simulation runtime of 500 Myr. The black lines represent the orbits of the 24 BHs that sink to the dense central region and grow into IMBHs. The orbits circularize as they decay, before finally plunging radially to the center (this last phase is not shown in the figure). Only BHs with an initial distance of $\lesssim$ 5pc from the center are found in this category. The dotted box region on the upper left demarcates the region in the a-e parameter space where we never found examples of BHs that successfully grow into a central massive BH. The dashed horizontal line marks the core radius at $r_{\rm c} = 0.003$ pc.

The red dots in Figure 3 represent the orbital evolution of BHs that do not make it to the dense central region to become IMBHs within the 500 Myr runtime of the simulations; the black curves represent the orbital evolution of BHs that do grow into IMBHs. The dotted box in the upper left approximately encloses initial orbital parameters (a and e) for BHs which do not grow to IMBH/SMBH. BHs with the initial a and e outside the box have sunk to the core and have experienced hyper-Eddington accretion, whereas we find no such examples with initial a and e that lie inside the box. Notice that some BHs with small initial semimajor axes (i.e. outside the box) migrate to the center after the first BH becomes massive, and form a bound pair with it. The dashed horizontal line near the bottom marks the core radius, $r_{\rm c} = 0.003$ pc.

BHs evolve from having large semimajor axes and high-eccentricity orbits (upper left of the panel) about the center of the protogalaxy potential, to having tighter, nearly circular orbits (lower right portion of the panel). As a BH approaches the center of the protogalaxy, it sinks to the center more quickly than it can complete an orbit.

The final plunge into the center of the protogalaxy is not plotted, as we find that e cannot be reliably calculated from the shape of the orbit.

The orbital evolution and the final transition to hyper-Eddington accretion described above can be understood as follows. Outside the core, the mass enclosed inside the BH orbit is $M_{\rm bg} \approx 4\pi\rho_{\rm c} r_{\rm c}^2 r \propto r$, and the dynamical time can be expressed as

$$\tau_{\rm dyn} = \left(\frac{r}{a_{\rm g}}\right)^{1/2} \approx 170 \left(\frac{r}{r_{\rm c}}\right)\ {\rm yr}\,. \quad (20)$$

Barring an encounter with another BH, BHs have velocities $v \sim c_{\rm s}$ or smaller. In this subsonic regime, $f^{\rm gas} v^{-3} \lesssim c_{\rm s}^{-3}$ in Eq. 9. Writing $a_{\rm df} \sim v/\tau_{\rm df}$, we can estimate $\tau_{\rm df}$ as

$$\tau_{\rm df} \sim (1-4) \times 10^3 \left(\frac{M}{10\ {\rm M}_\odot}\right)^{-1} \max\left[1, \left(\frac{r}{r_{\rm c}}\right)^2\right]\ {\rm yr}\,, \quad (21)$$

where the leading factor depends on whether the Mach number is less than or greater than $\mathcal{M} = 0.8$. The azimuthal force due to dynamical friction results in circularization and orbital decay on a timescale of $\tau_{\rm df}$, whereas in the radial direction the background force dominates over dynamical friction ($\sim$ Myr for pericenter passage of $\gtrsim 30\ r_{\rm c}$ and $M \sim 30\ {\rm M}_\odot$). Because $\tau_{\rm df} \propto r^2$ outside the core, the decay accelerates, with the final stages occurring over a few thousand years.

Since the orbital decay occurs on a timescale much shorter than the Salpeter time, the BH does not grow significantly by either sub-Eddington or Eddington-limited accretion. If $M \lesssim 60\ {\rm M}_\odot$, then $r_{\rm B} \lesssim r_{\rm c}$ and the orbital velocity is comparable to or less than the sound speed. The Bondi accretion rate for stellar-mass BHs outside the core can be estimated as

$$\begin{aligned}\dot{M}_{\rm B} &\approx \frac{4\pi G^2 M^2 \rho(r)}{c_{\rm s}^3} \\ &= 7 \times 10^{-3} \left(\frac{M}{10\ {\rm M}_\odot}\right)^2 \left(\frac{r}{r_{\rm c}}\right)^{-2}\ {\rm M}_\odot\ {\rm yr}^{-1} \\ &= 3.1 \times 10^5 \left(\frac{M}{10\ {\rm M}_\odot}\right) \left(\frac{r}{r_{\rm c}}\right)^{-2} \dot{M}_{\rm Edd}. \end{aligned} \quad (22)$$

Hence an infalling stellar-mass BH begins to undergo hyper-Eddington accretion when $r \gtrsim r_{\rm c}$.

3.2 Hyper-Eddington accretion: a brief but dramatic growth spurt

Once the BH overcomes the $\dot{M}_{\rm B} = 3000\ \dot{M}_{\rm Edd}$ threshold, its accretion rate instantaneously increases by a factor of $3000\ \eta = 300$. At the instant after this transition, its mass growth timescale is $M/\dot{M} \approx 0.1$ Myr (the Salpeter time divided by 3000η), but then rapidly shortens as $\propto M^{-1}$ before quickly hitting the ceiling $f_{\rm in}\dot{M}_{\rm in}$ imposed by the large-scale mass inflow rate (eq. 16). For comparison, note that in Eddington-limited growth, $\dot{M} \propto M$ and the growth timescale is constant at the Salpeter value. As a result, when the BH accretion rate becomes hyper-Eddington, its mass shoots up from a few $\times\ 10\ {\rm M}_\odot$ to more than $10^3\ {\rm M}_\odot$ in less than ~ 0.1 Myr.

This rapid mass growth results in two significant transitions in our simulations. First, the gas mass inside the Bondi radius exceeds that of the BH mass. Again, how the BH is assumed to accrete mass when $M_{\rm B} > M$ is what distinguishes our $f_{\rm in} = 1$, $f_{\rm in} = 10^{-3}$, $f_{\rm in} = 0$ and "I" models.

If $M \lesssim 60\ {\rm M}_\odot$, then the Bondi radius is small and the density at the surface of the Bondi sphere is close to the local density. Then, considering the Bondi-like profile ($\sim r^{-3/2}$) inside the Bondi sphere,

$$\begin{aligned} M_{\rm B} &\sim \int_0^{r_{\rm B}} \langle\rho_{\rm B}(r')\rangle \left(\frac{r_{\rm B}}{r'}\right)^{3/2}\ r'^2\ {\rm d}r' \quad (23) \\ &\sim \frac{8\pi}{3} r_{\rm B}^3 \rho(r) \\ &\sim 0.7\ {\rm M}_\odot \left(\frac{M}{10\ {\rm M}_\odot}\right)^3 \min\left[1, \left(\frac{r}{r_{\rm c}}\right)^{-2}\right], \quad (24) \end{aligned}$$

and $M_{\rm B} < M$.

However, since $r_{\rm B} \propto M$, at larger BH masses the Bondi sphere quickly becomes larger than the gaseous core. We just established above that the BH typically begins its hyper-Eddington accretion near the core. Therefore, once a BH grows to $M \gtrsim 60\ {\rm M}_\odot$, $r_{\rm B} > r_{\rm c}$ and the gas density at the surface of the Bondi sphere is essentially given by the halo gas profile evaluated at $r = r_{\rm B}$. Then we can write

$$M_{\rm B} \sim \frac{8\pi}{3} r_{\rm B}^3 \rho(r_{\rm B}) \approx \frac{8\pi}{3} \rho_{\rm c} r_{\rm c}^2 r_{\rm B} = 2.4M > M. \quad (25)$$

We conclude that as soon as hyper-Eddington accretion begins, the gas enclosed inside the Bondi sphere shoots above the BH mass.

The second transition that occurs as the BH grows is that the BH mass exceeds the mass of the matter enclosed inside its orbit around the center of the halo ($M_{\rm bg}$). For $r \gg r_{\rm c}$, the enclosed mass is simply

$$M_{\rm bg} \gtrsim 4\pi\rho_{\rm c} r_{\rm c}^2 r \approx 200\ {\rm M}_\odot \left(\frac{r}{r_{\rm c}}\right), \quad (26)$$

whereas inside the core ($r \ll r_{\rm c}$)

$$M_{\rm bg} = \frac{4\pi}{3}\rho_{\rm c} r^3 \approx 70\ {\rm M}_\odot \left(\frac{r}{r_{\rm c}}\right)^3. \quad (27)$$

Either way, as the BH grows beyond several $100\ {\rm M}_\odot$ near or inside the core, our simulations always result in $M > M_{\rm bg}$. Since the BH dominates the central potential, the innermost gas distribution will be strongly disturbed, and will correspond to a radial force towards the center of the halo. This is the motivation for running a second set of simulations, in which the gravitational force of the background matter is turned off if $M > M_{\rm bg}$.

The above caveats aside, the hyper-Eddington rate initially follows the Bondi rate and scales as $\dot{M} \propto M^2$. One significant aspect of this mode of growth is that, in addition to the raw accretion rate being much higher than Eddington-limited growth, the accretion timescale decreases (i.e. the growth rate accelerates and is faster than exponential). However, this growth does not last long in our simulations, because $\dot{M}$ encounters one of two upper limits.

The first upper limit is $f_{\rm in}\dot{M}_{\rm in}$ (where $\dot{M}_{\rm in} = c_{\rm s}^3/G$), the parameterized gas supply rate into the center of the halo in the "$f_{\rm in} = 1$","$f_{\rm in} = 10^{-3}$", and "$f_{\rm in} = 0$" models.

The second one is due to the fact that as M increases, $r_{\rm B}$ increases, and the density at the surface of the Bondi sphere decreases. For $r_{\rm B} \gg r$ and $r_{\rm B} \gg r_{\rm c}$, the density at

the Bondi sphere surface becomes

$$\rho(r_{\rm B}) \approx \rho_{\rm c} \left(\frac{r_{\rm B}}{r_{\rm c}}\right)^{-2} = \frac{\rho_{\rm c} r_{\rm c}^2 c_{\rm s}^4}{4G^2M^2}. \quad (28)$$

Then the Bondi accretion rate evaluates to

$$\dot{M}_{\rm B} = \frac{4\pi G^2 M^2 \rho(r_{\rm B})}{c_{\rm s}^3(1+\mathcal{M}^2)^{3/2}} \approx \pi \rho_{\rm c} r_{\rm c}^2 c_{\rm s} \approxeq 0.2\ {\rm M}_\odot\ {\rm yr}^{-1}, \quad (29)$$

or ≈ 40 % of $\dot{M}_{\rm in}$ ($=c_{\rm s}/G^3$).

To summarize, the dynamics in our simulations evolves according to the following trends:

(i) The orbit of the innermost BH decays on the dynamical friction timescale. As it does, the accretion rate goes from sub-Eddington Bondi-Hoyle-Littleton ($\dot{M} \propto M^2$, $\dot{M} \leqslant \dot{M}_{\rm Edd}/\eta$) to Eddington-limited accretion ($\dot{M} = \dot{M}_{\rm Edd}/\eta \propto M$). However, this phase lasts much less than a Salpeter time, and the mass growth is typically insignificant.

(ii) As the BH approaches the center of the halo, typically at $r \sim$ a few $\times\, r_{\rm c}$, the Bondi rate $\dot{M}_{\rm B} > 3000\dot{M}_{\rm Edd}$. At this point, following IHO16, we assume that photon trapping allows for hyper-Eddington accretion, i.e. once again matching the unimpeded BHL rate ($\dot{M} = \dot{M}_{\rm B} \propto M^2$).

(iii) In the hyper-Eddington phase, the BH grows from a typical mass of a few $\times 10$ M$_\odot$ to $\gtrsim 10^3$ M$_\odot$. During this rapid transition, the BH becomes more massive than the mass contained inside its orbit around the halo center ($M > M_{\rm bg}$), and the gas mass enclosed within its Bondi sphere exceeds its own mass ($M_{\rm B} > M$). The behaviour up to this point is almost identical for all the simulations that allow for hyper-Eddington accretion (models "$f_{\rm in} = 1$","$f_{\rm in} = 10^{-3}$","$f_{\rm in} = 0$" and "I"). Most of the variation between these models result from the difference in prescriptions when $M_{\rm B} > M$ and $M > M_{\rm bg}$. That is, the models "branch out" from this point forward.

(iv) The accretion rate then slows, as it encounters the halo mass supply limit $f_{\rm in}\dot{M}_{\rm in}$ or the asymptotic constant value of $\dot{M}_{\rm B}$ in the limit of large Bondi radius. Because both of these values are constant, as the BH mass increases $\dot{M}$ falls below $3000\dot{M}_{\rm Edd} \propto M$, and becomes Eddington-limited again. The final masses of the BHs, and their configuration with respect to the halo and other BHs, depend on the prescriptions for accretion and background gravitational force, as discussed in the following.

3.3 The final IMBH masses and configurations

In Table 3, we summarize the average final masses and accretion rates found in our simulations, for each combination of our prescriptions for gas accretion and treatment of the background gravitational force. The values presented are the mean values over the 24 realizations per model with a nuclear BH, evaluated when the first BH has sunk to the center of the protogalaxy and has captured a companion BH into a closed orbit with a semimajor axis ≈ 1 pc. We have chosen to stop the simulations at $a = 1$ pc, because at smaller separations between the innermost bound pair three-body scatterings are rare. We assume that past this separation, the inner bound pairs evolve through damped, closed orbits until merger. masses and instantaneous accretion rates of the central BH are denoted with a subscript "1," and those for the smaller companion BH with a subscript "2." We also list the mass ratio $M_2/M_1 \leqslant 1$ and the orbital eccentricity e of the pair.

The bottom half of Table 3 lists the BH properties found in simulations where the background gravitational force exerted on a given BH was set to zero whenever the BH mass exceeded the mass enclosed inside its radial position. The final values found in these simulations do not vary significantly from the ones in which the background force was always present (the top half of the table).

3.3.1 The central BH

Let us first discuss the central BH. In the simulations with $f_{\rm in} = 0$, BHs stop growing once they are outweighed by the gas mass enclosed inside their Bondi sphere. Because of this, they never grow beyond $M_1 \sim 100$ M$_\odot$. In simulations where $f_{\rm in} = 10^{-3}$, $f_{\rm in} = 1$, and "I" the growth rate is capped by $f_{\rm in}\dot{M}_{\rm in}$ and by the asymptotic Bondi rate (eq. 29). These upper bounds allow the growth of the central BH to $M_1 \sim 10^4$ M$_\odot$ for $f_{\rm in} = 10^{-3}$, and $M_1 \sim 10^5$ M$_\odot$ to $\sim 10^6$ M$_\odot$ for $f_{\rm in} = 1$ and "I" (note that the values for $f_{\rm in}\dot{M}_{\rm in}$ and the asymptotic Bondi rate are comparable). *In all simulations where hyper-Eddington accretion is allowed to continue past the point $M < M_{\rm B}$, the central BH grows into an IMBH or SMBH.*

For reference, we can see that if the mass growth is limited at the canonical Eddington value (model "E"), then the central BH which forms a bound pair with another BH does not grow significantly. This is because the bound pairs reach $a \lesssim 1$ pc soon after the first BH sinks to the core, when both BHs are still close to their original stellar masses. Once a tight central binary forms, its orbital velocity increases, and suppresses the BHL accretion rate below the Eddington value, stunting further growth of either BH. We also show, for reference, values in which accretion is not allowed at all (model "$\dot{M} = 0$").

3.3.2 The stellar-mass BH companion

A striking result of our simulations is that we find no more than one hyper-accreting BH per simulation (i.e. either zero or one IMBH per galaxy). The reason for this is that if an IMBH forms in one of our simulations, it prevents other BHs from undergoing hyper-Eddington accretion.

This finding can be explained as follows. The first IMBH forms relatively quickly (its orbit decays in a few Myr), and does so at the center of the halo, where gas densities (and Bondi accretion rates) are high. Once this IMBH is in the center of the halo, any subsequent BH whose orbit decays will be captured by the IMBH potential. Whereas the first BH had orbital velocities $v \lesssim c_{\rm s}$ as it fell toward the center, the orbital velocity of a BH captured by the IMBH will be supersonic. The supersonic orbital motion suppresses both the orbital decay rate via dynamical friction, preventing the second BH from sinking deep into the gas-rich center of the halo. On top of this, the high velocity suppresses the Bondi-Hoyle-Lyttleton accretion rate, $\dot{M}_{\rm B} \propto (c_{\rm s}^2 + v^2)^{-3}$.

Thus, the first BH to wander to the center of the potential is able to grow to an IMBH via hyper-Eddington accretion, but then *subsequently prevents other BHs from doing the same.* As a result, our simulations typically produce

Table 3. Average mass, mass ratio, eccentricity (e) and accretion rate for the first BH-BH pair when its semimajor axis is $a \approx 1$ pc. Accretion rates are in units of the Eddington rate. The subscript "1" refers to the more massive BH, and "2" to the less massive BH.

$a_{\rm bg}$	Model	$M_1[\,{\rm M}_\odot]$	$M_2[\,{\rm M}_\odot]$	$q\ (=M_2/M_1)$	e	$\dot{M}_1/\dot{M}_{\rm Edd,1}$	$\dot{M}_2/\dot{M}_{\rm Edd,2}$
on	$f_{\rm in}=0$	160	71	0.45	0.92	0	38000
	$f_{\rm in}=10^{-3}$	1.5×10^4	45	3.0×10^{-3}	0.99	19	4.8
	$f_{\rm in}=1$	6.1×10^5	31	5.1×10^{-5}	0.90	760	8.6×10^{-2}
	I	2.5×10^5	38	1.5×10^{-4}	0.87	10	2.9
	E	450	50	0.11	0.99	10	5.9
	$\dot{M}=0$	41	37	0.92	0.96	0	0
off	$f_{\rm in}=0$	170	91	0.55	0.92	0	58000
	$f_{\rm in}=10^{-3}$	2.6×10^4	44	1.7×10^{-3}	0.99	17	3.2
	$f_{\rm in}=1$	4.1×10^6	29	7.0×10^{-6}	0.84	240	2.1×10^{-2}
	I	2.7×10^6	33	1.2×10^{-5}	0.98	10	0.78
	E	370	53	0.14	0.90	10	6.8
	$\dot{M}=0$	41	37	0.92	0.87	0	0

bound pairs of IMBHs and stellar-mass BHs with mass ratios $q \equiv M_1/M_2 \sim 10^{-4}-10^{-2}$. Such "extreme mass-ratio" systems are one of the important targets for detection by planned gravitational-wave instruments, and we will revisit them in our discussion section. As Table 3 shows, interestingly, all EMRIs have a highly eccentric orbit; this is a result of the preferential capture of stellar-mass BHs on such orbits, i.e. with pericenters inside the sphere of influence of the newly grown IMBH.

In models where an IMBH is not produced, subsequent BHs are free to fall to the center at low speeds, just as the first one did. As shown in Table 3, in the "$f_{\rm in}=0$" models, we find near-equal, stellar-mass binaries forming in the nucleus. In these models, the growth of the 1st BH is artificially stunted, allowing the 2nd BH to experience a brief phase of hyper-Eddington accretion. This hyper-Eddington phase, as the 2nd BH travels through the dense gaseous core, only lasts until it, too, reaches a mass of $M_2 \gtrsim 100$ M$_\odot$; its Bondi sphere will then become self-gravitating, and its grow is terminated, just as for the first BH.

3.3.3 Different treatments of central background potential

The main difference in the two sets of models (shown in the bottom vs. top half of Table 3) is that if $a_{\rm bg}$ is always present, the central BH ends up at the very center of the model protogalaxy, because the background force always continues to point inward. In contrast, when $a_{\rm bg}$ is turned off, the gas drag brings the BHs to rest near—but not *at*—the center. Aside from this detail, we find no major qualitative difference in the properties of the BHs across these two sets of simulations. We conclude that the hydrodynamical reaction of the innermost gas to the central BH is unlikely to significantly influence our main conclusions about the demography and location of the emerging BH population (in particular whether hyper-Eddington accretion occurs).

4 DISCUSSION

4.1 SMBH precursors

Our simulations focus on the growth and orbital evolution of Pop III remnant BHs in a model protogalaxy that is just above the atomic-cooling threshold for virial mass. We find that the hyper-Eddington accretion prescription of IHO16 typically results in the formation of a single IMBH in the center of the protogalaxy.

The natural interpretation is that this is a massive nuclear BH that will continue to grow as the host galaxy grows. The formation of a $\sim (10^4-10^5)$ M$_\odot$ BH in an atomic-cooling halo is the same end result as in the so-called "direct collapse BH" scenario. These IMBHs must then grow at a logarithmically time-averaged rate $\dot{M} \lesssim 10\dot{M}_{\rm Edd}$ (i.e. at a rate comparable to the Eddington limit for a radiative efficiency $\eta \sim 0.1$) to explain the $\gtrsim 10^9$ M$_\odot$ engines of the $z \gtrsim 6$ quasars. The direct collapse scenarios generically require specific conditions that may be rare in the Universe. For example, in most models the collapse is facilitated by a high Lyman-Werner intensity that dissociates molecular hydrogen, and thus only a small fraction of galaxies are expected to be viable direct-collapse sites (e.g. Dijkstra et al. 2008; Shang, Bryan & Haiman 2010; Hosokawa, Omukai & Yorke 2012; Dijkstra, Ferrara & Mesinger 2014; Sugimura, Omukai & Inoue 2014; Visbal, Haiman & Bryan 2014; Latif et al. 2015; Inayoshi & Tanaka 2015; Regan, Johansson & Wise 2016).

The picture suggested by our simulations is that IMBHs in protogalactic nuclei could plausibly be more commonly produced by hyper-Eddington growth of a pre-existing stellar-mass BH – the essential requirements being only a high-density core, and a large-scale inflow rate of $O(\,{\rm M}_\odot{\rm yr}^{-1})$, down to the Bondi radius ($\sim$0.01 pc) of the central BH with initial mass of ~ 100 M$_\odot$.

These two hypotheses for SMBH progenitors—rare direct-collapse seeds and more common results of hyper-Eddington accretion—could be tested against observations through event rates detected by milli-Hertz gravitational-

wave detectors (e.g. Sesana, Volonteri & Haardt 2007; Tanaka & Haiman 2009) or by the global signatures of the redshifted 21 cm line (e.g. Tanaka, O'Leary & Perna 2016).

4.2 EMRI detections

Whenever an IMBH forms in our simulations, we find that it captures one or more stellar-mass BH companions. Mergers of such BHs are predicted to produce EMRIs, a category of gravitational wave events that is one of the primary *low-redshift* targets of the space-based interferometer *eLISA* (Consortium et al. 2013; Amaro-Seoane et al. 2013).

Because the timescale for the $M_2 \ll M_1$ pairs in our simulations to merge through emission of gravitational waves is well over a Hubble time, additional mechanisms such as three-body scatterings or continuous gaseous dissipation (e.g. by a circumbinary accretion disc, Cuadra et al. 2009; Roedig et al. 2011) are required to drive the merger. The production of such pairs in our simulations suggests that they could result in mergers of IMBHs and stellar-mass BHs at lower redshifts.

We note that our IMBH-BH pairs have eccentricities $e \gtrsim 0.9$, at $a \approx 1$ pc (Table 3). This points to the interesting possibility that they could lead to EMRIs that have residual eccentricities when they enter the eLISA band. However, as we do not follow the evolution of such pairs all the way to merger, and given the variety of possibly relevant mechanisms, we leave the assessment of any residual eccentricity in the eLISA band for future work.

Additionally, the merger of a protogalaxy or dwarf galaxy containing an IMBH with a more massive one containing a SMBH should result in the formation of a SMBH-IMBH pair. While this is an expected corollary of our findings, further work is required to assess whether such pairs can overcome the so-called "final parsec problem" (Merritt & Milosavljević 2005).

4.3 Comparison with previous work

Several recent papers have investigated super-Eddington accretion in galaxies. Lupi et al. (2016) used hydrodynamical simulations to investigate super-Eddington accretion of stellar-mass BHs in circumnuclear gas discs in the hearts of galaxies. Their scheme allows gas particles close to the BH to accrete and grow the BH. Pezzulli, Valiante & Schneider (2016) considered the growth of stellar-mass BHs inside model galaxies that account for metal enrichment, dust, star formation and detailed cooling. They assume that the central BH grows at a rate proportional to the cold gas mass in the bulge, and inversely proportional to the dynamical time of the bulge.

One major difference between this study and those papers is the accretion prescription. We adopt the analytic Bondi-like accretion prescription based on IHO16 and featuring the transition from low Bondi-Hoyle-Lyttleton accretion, to Eddington-limited accretion, and then to hyper-Eddington accretion. Another notable difference is that Lupi et al. (2016) and Pezzulli, Valiante & Schneider (2016) examined the growth of BHs in fully evolved galaxies, whereas in this study we focus on the growth of Pop III remnant BHs into IMBHs in a protogalaxy of mass $\sim 10^8$ $M_\odot$.

Alexander & Natarajan (2014) considered a set-up similar to ours, in which a stellar-mass BH is in orbit in a protogalaxy, accreting above the fiducial Eddington rate. The focus of that paper was to assess the ability of the gas inside the BH's sphere of influence to shed angular momentum and accrete onto the BH. The orbit of the BH was assumed to be determined by its interactions with a nuclear star cluster (which was found to be important to reduce the angular momentum). Here we treated a small system of BHs, and assumed that the background gas dominates their orbital decay into the nucleus.

Closest to our study, Tagawa et al. (2015) and Tagawa, Umemura & Gouda (2016) performed N-body simulations of BHs embedded in a compact distribution of gas, in order to gauge the merger mechanisms of BHs in galactic centers. Overall, the set-up and goals of these studies and ours are similar, although Tagawa et al.'s focus was to clarify the occurrence rate and mechanisms of stellar-mass BH mergers. Our most notable finding – the frequent formation of a *single IMBH* at the *center* of the protogalaxy – differs from the conclusions by Tagawa et al. (2015) and Tagawa, Umemura & Gouda (2016), who find efficient formation of stellar-mass binaries, often facilitated by 3-body interactions.

These differences in conclusions arise from three important differences between our initial conditions and model assumptions. First, we spread 10 initial BHs over a large region of up to 100 pc, with separations of > 10 pc. The initial BH separations are much more compact in Tagawa et al. (2015, $0.01 - 10$ pc) and especially in Tagawa, Umemura & Gouda (2016, $0.01 - 0.1$ pc). As a result, we do not find 3-body interactions or stellar-mass binaries. Second, we adopt a centrally condensed density profile, while Tagawa et al. (2015) and Tagawa, Umemura & Gouda (2016) both assume homogeneous clouds. Third, we investigate various accretion prescriptions, and allow hyper-Eddington accretion at rates limited only by the steady large-scale inflow rate (whereas Tagawa et al. (2015) did not consider accretion onto BHs and Tagawa, Umemura & Gouda (2016) considered an accretion rate capped by the Eddington limit and by the assumed total cloud mass). As a result of these last two differences, we find that rapid growth into IMBHs and SMBHs is much more common, and always occurs in the nucleus – producing EMRIs, rather than stellar-mass binaries.

4.4 Caveats

Our results were obtained in simplified toy models, and are subject to several caveats. We here discuss three possible major limitations of our model.

Gravitational potential of the background matter. Our simulations assume a static density profile of gas and dark matter, instead of allowing the protogalaxy to evolve dynamically or thermodynamically. On one hand, the simplified treatment of the protogalaxy allowed us to run hundreds of simulations—dozens of initial condition realizations for each of a dozen different combinations of theoretical models. On the other, this survey of model prescriptions and the statistical sample size came at the expense of a more detailed treatment of gas dynamics.

In particular, not accounting for the dynamical evolution of the surrounding matter directly impacts the two

gravitational effects in this work: the gravitational force exerted by the ambient matter, and dynamical friction. Our assumption of a static background allows us to evaluate analytically the gravitational force from the ambient medium, and we treat the dynamical friction using a modified version of the Chandrasekhar formula (Binney & Tremaine 1987).

In an attempt to gauge the robustness of our results with respect to these theoretical simplifications, we ran different sets of simulations with very different assumptions. First, as discussed above, we ran a set of simulations in which the gravitational field of the background material was entirely removed, once the BH mass exceeded the mass of the matter enclosed inside its orbit. The only qualitative difference we found was that this resulted in the central BH ending up slightly off-center (whereas leaving the analytic background force "on" had the effect of always pulling the central BH to the very center of our model protogalaxy). We also note that while gas anisotropies are common features in simulations of protogalactic haloes, the masses of any anisotropic clumps tend to be small compared to that of the ambient gas (which are overall well-described by power-law profiles, e.g. Regan & Haehnelt 2009b).

We also ran, for the same set of the different accretion prescriptions, simulations in which the dynamical friction was not calculated using the local gas density at the BH coordinates $\rho(r)$, but using the gas density averaged over the surface of its Bondi sphere, $\langle \rho_{\rm B}(r) \rangle$. The rationale behind this experiment was that whereas the derivation of the Chandrasekhar formula assumes an infinite, uniform background distribution of gas, the physical phenomenon of dynamical friction is due to the wake of overdense gas formed at some distance from the massive body. We found no qualitative difference between this set of simulations and the one described in §3. While there is a rich literature on quantifying how dynamical friction differs in nonuniform density distributions or nonlinear trajectories (e.g Sánchez-Salcedo & Brandenburg 2001; Just & Peñarrubia 2005; Kim & Kim 2007; Kim 2010), these studies do not report major differences from the Chandrasekhar formula.

We conclude that our results are unlikely to be an artifact of the simplified treatment of the gravity of the ambient matter distribution.

Star formation in the halo. Our model does not consider star formation inside the halo. Once a dense region of gas cloud in the halo becomes optically thick, fragmentation leads to star formation (e.g. Regan, Johansson & Haehnelt 2014; Becerra et al. 2015, and refs. therein). The stars may form directly in the core region, or form elsewhere and subsequently migrate to the core. Because the stars have lifetimes of $\sim$ Myr, we expect them to become BHs before arriving at the core, or shortly afterward. In practice, we do not expect significant qualitative differences based on which type of BH reaches the core first—the pre-existing BHs our simulations had in mind, or the stars/BHs that form in situ in the halo. According to the picture suggested by our simulations, whichever type of BH arrives at the center first should grow massive via hyper-Eddington accretion, then capture any subsequent arrivals into bound orbits (which may eventually produce EMRI events).

Therefore, we do not expect any in situ star formation in the halo to qualitatively affect our findings.

Effect of radiation on the hydrodynamics. Our toy model neglects the radiation produced by the accreting BHs (and of any stars found in the same galaxy). The gas in the halo cools efficiently and is mostly neutral, and accreting BHs will create their individual small HII regions. Here we estimate the size of these HII regions, before the BHs wander into the core and reach the hyper-Eddington state. In the "intermediate" regime, when $\eta^{-1} \lesssim \dot{M}_{\rm B}/\dot{M}_{\rm Edd} \lesssim 3000$, the time-averaged accretion rate is limited to the Eddington rate, because of the periodic formation, disappearance, and re-appearance, of an HII region that makes the accretion episodic. The maximum size of this HII region is larger than the Bondi radius, by definition, before the hyper-Eddington state can be reached (IHO16). Assuming a luminosity of $L_{\rm Edd}$, the HII region size is $R_{\rm HII} = 8 \times 10^{13} (M/30\ {\rm M}_\odot)^{1/3} (r/r_c)^{4/3}$cm (see eq. 27 in IHO16) or $R_{\rm HII}/r = 0.01 (M/30\ {\rm M}_\odot)^{1/3} (r/r_c)^{1/3}$. This means that the HII region remains relatively small for BHs located within a few pc of the core. A near-Eddington BH outside this region (say at 10-100 pc) could blow a large HII bubble and change the global density distribution. However, the stellar-mass BHs in these outer, low-density regions will be highly sub-Eddington and dim (eq. 22). We conclude that radiative feedback is unlikely to prevent the onset of the hyper-Eddington phase of the first BH that sinks to the central region.

Validity of Hyper-Eddington accretion. As emphasized throughout this paper, a key ingredient of our model is that we allow rapid accretion, well in excess of $L_{\rm Edd}/c^2$. This is based on the recent results of IHO16, who find this to be the case for accreting BHs whose HII region is confined to within the Bondi radius. This conclusion is subject to a few caveats summarized in IHO16. In particular, here we highlight the fact that IHO16 assumes a spherically symmetric accretion flow with low angular momentum, such that the centrifugal radius (setting the size of an accretion disc, producing significant luminosity) is smaller than the trapping radius (inside which photons are advected inward with the flow, rather than diffusing out). At the onset of the hyper-Eddington phase, the latter is 1500 $R_{\rm Sch}$, or $5 \times 10^{10} (M/100\ {\rm M}_\odot)$ cm. We thus require that the accretion flow onto the BHs remain quasi-spherical down to this distance from the BH. While this appears feasible once the BH settles to the bottom of the potential well, a proper assessment will require follow-up investigations, resolving the angular momentum transfer and dissipation for the flow onto the central BH. However, we note here that this requirement is much less stringent than the one addressed in a similar context by Alexander & Natarajan (2014), who required the centrifugal radius to be as small as a few $\times R_{\rm Sch}$ (and found it to be feasible, faciliated in their model by resonant effects due to a central stellar cluster).

5 SUMMARY

In this paper, we described the formation of 10^{3-5} ${\rm M}_\odot$ IMBHs in centrally condensed gas clouds, arising from a small cluster of Population III remnant black holes (BHs). The stellar-mass BH are assumed to have been delivered into the cloud during the process of the hierarchical assembly of the halo via mergers, and have a spatially extended initial configuration (several pc to 100 pc). We then follow their

accretion and orbital dynamics via an N-body calculation. These calculations reveal that as a result of gas drag, one of these BHs typically sinks to the nucleus, where it rapidly grows into an IMBH.

Our results suggest a viable pathway to forming the earliest massive BHs in the centers of early galaxies. We also find that only one IMBH can form in this way per galaxy, and that this IMBH typically captures a stellar-mass BH companion, making these systems observable in gravitational waves as extreme mass-ratio inspirals (EMRIs) with *eLISA*.

More detailed simulations that account for the hydrodynamics, radiative transfer, and the cosmological evolution of the host protogalaxy are required to test this idea further.

Acknowledgements Results in this paper were obtained using the high-performance LIred computing system at the Institute for Advanced Computational Science at Stony Brook University, which was obtained through the Empire State Development grant NYS #28451. This work was supported in part by NASA grants NNX11AE05G and NNX15AB19G (ZH).

REFERENCES

Abramowicz M. A., Czerny B., Lasota J. P., Szuszkiewicz E., 1988, ApJ, 332, 646
Agarwal B., Khochfar S., Johnson J. L., Neistein E., Dalla Vecchia C., Livio M., 2012, M.N.R.A.S., 425, 2854
Alexander T., Natarajan P., 2014, Science, 345, 1330
Alvarez M. A., Wise J. H., Abel T., 2009, ApJL, 701, L133
Amaro-Seoane P. et al., 2013, GW Notes, Vol. 6, p. 4-110, 6, 4
Becerra F., Greif T. H., Springel V., Hernquist L. E., 2015, M.N.R.A.S., 446, 2380
Begelman M. C., 1979, M.N.R.A.S., 187, 237
—, 2012, M.N.R.A.S., 420, 2912
Begelman M. C., Volonteri M., Rees M. J., 2006, M.N.R.A.S., 370, 289
Binney J., Tremaine S., 1987, Galactic dynamics. Princeton University Press
Blecha L., Cox T. J., Loeb A., Hernquist L., 2011, M.N.R.A.S., 412, 2154
Bromm V., Loeb A., 2003, ApJ, 596, 34
Chapon D., Mayer L., Teyssier R., 2013, M.N.R.A.S., 429, 3114
Consortium T. e. et al., 2013, ArXiv e-prints
Cuadra J., Armitage P. J., Alexander R. D., Begelman M. C., 2009, M.N.R.A.S., 393, 1423
Damour T., Deruelle N., 1981, Physics Letters A, 87, 81
Dijkstra M., Ferrara A., Mesinger A., 2014, M.N.R.A.S., 442, 2036
Dijkstra M., Haiman Z., Mesinger A., Wyithe J. S. B., 2008, M.N.R.A.S., 391, 1961
Erwin F., 1969, NASA Technical Report, 315, 1
Escala A., Larson R. B., Coppi P. S., Mardones D., 2004, ApJ, 607, 765
Fabian A. C., 2012, Ann. Rev. A&A, 50, 455
Fan X. et al., 2001, AJ, 122, 2833
Guedes J., Madau P., Mayer L., Callegari S., 2011, ApJ, 729, 125
Haiman Z., 2013, in Astrophysics and Space Science Library, Vol. 396, Astrophysics and Space Science Library, Wiklind T., Mobasher B., Bromm V., eds., p. 293
Haiman Z., Loeb A., 2001, ApJ, 552, 459
Heger A., Fryer C. L., Woosley S. E., Langer N., Hartmann D. H., 2003, ApJ, 591, 288
Hosokawa T., Omukai K., Yorke H. W., 2012, ApJ, 756, 93
Hosokawa T., Omukai K., Yoshida N., Yorke H. W., 2011, Science, 334, 1250
Inayoshi K., Haiman Z., Ostriker J. P., 2015, MNRAS, submitted; e-print arXiv:1511.02116
Inayoshi K., Tanaka T. L., 2015, M.N.R.A.S., 450, 4350
Just A., Peñarrubia J., 2005, A&A, 431, 861
Kim H., Kim W.-T., 2007, ApJ, 665, 432
Kim W.-T., 2010, ApJ, 725, 1069
Kormendy J., Ho L. C., 2013, Ann. Rev. A&A, 51, 511
Koushiappas S. M., Bullock J. S., Dekel A., 2004, M.N.R.A.S., 354, 292
Kupi G., Amaro-Seoane P., Spurzem R., 2006, M.N.R.A.S., 371, L45
Latif M. A., Bovino S., Grassi T., Schleicher D. R. G., Spaans M., 2015, M.N.R.A.S., 446, 3163
Latif M. A., Schleicher D. R. G., Schmidt W., 2014, M.N.R.A.S., 440, 1551
Latif M. A., Schleicher D. R. G., Schmidt W., Niemeyer J., 2013, M.N.R.A.S., 433, 1607
Lodato G., Natarajan P., 2006, M.N.R.A.S., 371, 1813
Lupi A., Haardt F., Dotti M., Fiacconi D., Mayer L., Madau P., 2016, M.N.R.A.S., 456, 2993
Madau P., Haardt F., Dotti M., 2014, ApJL, 784, L38
Madau P., Rees M. J., 2001, ApJL, 551, L27
Madau P., Rees M. J., Volonteri M., Haardt F., Oh S. P., 2004, ApJ, 604, 484
Magorrian J., Tremaine S., Gebhardt K., Richstone D., Faber S., 1996, in Bulletin of the American Astronomical Society, Vol. 28, American Astronomical Society Meeting Abstracts, p. 1423
Merloni A., Heinz S., 2008, M.N.R.A.S., 388, 1011
Merritt D., Milosavljević M., 2005, Liv. Rev. Rel., 8, 8
Milosavljević M., Bromm V., Couch S. M., Oh S. P., 2009, ApJ, 698, 766
Mortlock D. J. et al., 2011, Nat., 474, 616
Navarro J. F., Frenk C. S., White S. D. M., 1997, ApJ, 490, 493
Oh S. P., Haiman Z., 2002, ApJ, 569, 558
Ostriker E. C., 1999, ApJ, 513, 252
Pacucci F., Ferrara A., 2015, M.N.R.A.S., 448, 104
Pacucci F., Volonteri M., Ferrara A., 2015, M.N.R.A.S., 452, 1922
Park K., Ricotti M., 2012, ApJ, 747, 9
Peters P. C., 1964, Physical Review, 136, 1224
Peters P. C., Mathews J., 1963, Physical Review, 131, 435
Pezzulli E., Valiante R., Schneider R., 2016, M.N.R.A.S.
Prieto J., Escala A., 2015, ArXiv e-prints
Regan J. A., Haehnelt M. G., 2009a, M.N.R.A.S., 396, 343
—, 2009b, M.N.R.A.S., 396, 343
Regan J. A., Johansson P. H., Haehnelt M. G., 2014, M.N.R.A.S., 439, 1160
Regan J. A., Johansson P. H., Wise J. H., 2016, M.N.R.A.S., submitted, e-print arXiv:1603.06612
Ricotti M., Ostriker J. P., 2004, M.N.R.A.S., 352, 547

Roedig C., Dotti M., Sesana A., Cuadra J., Colpi M., 2011, M.N.R.A.S., 415, 3033
Ryu T., Tanaka T. L., Perna R., 2016, M.N.R.A.S., 456, 223
Sánchez-Salcedo F. J., Brandenburg A., 2001, M.N.R.A.S., 322, 67
Schleicher D. R. G., Spaans M., Glover S. C. O., 2010, ApJL, 712, L69
Sesana A., Volonteri M., Haardt F., 2007, M.N.R.A.S., 377, 1711
Shang C., Bryan G. L., Haiman Z., 2010, M.N.R.A.S., 402, 1249
Shankar F. et al., 2016, M.N.R.A.S., submitted, e-print arXiv:1603.01276
Shankar F., Crocce M., Miralda-Escudé J., Fosalba P., Weinberg D. H., 2010, ApJ, 718, 231
Shapiro S. L., 2005, ApJ, 620, 59
Silk J., Rees M. J., 1998, A&A, 331, L1
Spaans M., Silk J., 2006, ApJ, 652, 902
Stacy A., Bromm V., 2013, M.N.R.A.S., 433, 1094
Sugimura K., Omukai K., Inoue A. K., 2014, M.N.R.A.S., 445, 544
Tagawa H., Umemura M., Gouda N., 2016, MNRAS, submitted; e-print arXiv:1602.08767
Tagawa H., Umemura M., Gouda N., Yano T., Yamai Y., 2015, M.N.R.A.S., 451, 2174
Tanaka T., Haiman Z., 2009, ApJ, 696, 1798
Tanaka T., Perna R., Haiman Z., 2012, M.N.R.A.S., 425, 2974
Tanaka T. L., 2014, Classical and Quantum Gravity, 31, 244005
Tanaka T. L., Li M., 2014, M.N.R.A.S., 439, 1092
Tanaka T. L., O'Leary R. M., Perna R., 2016, M.N.R.A.S., 455, 2619
Venemans B. P. et al., 2013, ApJ, 779, 24
Visbal E., Haiman Z., Bryan G. L., 2014, M.N.R.A.S., 445, 1056
Volonteri M., 2010, A&A Rev., 18, 279
Volonteri M., Rees M. J., 2005, ApJ, 633, 624
—, 2006, ApJ, 650, 669
Volonteri M., Silk J., Dubus G., 2015, ApJ, 804, 148
Willott C. J. et al., 2010, AJ, 139, 906
Willott C. J., McLure R. J., Jarvis M. J., 2003, ApJL, 587, L15
Wise J. H., Abel T., 2007, ApJ, 665, 899
—, 2008, ApJ, 685, 40
Yoo J., Miralda-Escudé J., 2004, ApJL, 614, L25
Zhang W., Woosley S. E., Heger A., 2008, ApJ, 679, 639